Geochemistry Geophysics Geosystems G3

Research Letter
Volume 12, Number 1
27 January 2011
Q01006, doi:10.1029/2010GC003358
ISSN: 1525-2027

Published by AGU and the Geochemical Society

Imaging the seismic lithosphere-asthenosphere boundary of the oceanic plate

Prakash Kumar
Earthquake Research Institute, University of Tokyo, 1-1-1 Yayoi, Bunkyo-ku, Tokyo 113-0032, Japan

On leave from National Geophysical Research Institute, Council of Scientific and Industrial Research, Uppal Road, Hyderabad 500 007, India

Hitoshi Kawakatsu
Earthquake Research Institute, University of Tokyo, 1-1-1 Yayoi, Bunkyo-ku, Tokyo 113-0032, Japan (hitosi@eri.u-tokyo.ac.jp)

[1] The seismic lithosphere-asthenosphere boundary (LAB) or G discontinuity, a seismologically characterized abrupt drop in wave speed in the uppermost mantle, is one of the key issues in current geodynamics. Although plate tectonics started as a theory for the ocean, reports on LAB for normal oceanic regions are scarce due to paucity of seismic data, and whether or not the oceanic LAB grows with age is the key issue to be resolved. We conduct a systematic survey for the oceanic LAB using *S*-to-*p* converted seismic waves along three margins of oceanic plates whose crustal age ranges from ~10 Myr to ~130 Myr, and we observe laterally continuous oceanic LAB images. The thickness of the oceanic plate estimated from LABs increases with the plate age, though scattered, suggesting that the evolution of oceanic lithosphere is predominantly governed by temperature and that the oceanic seismic LAB represents a boundary that grows with age.

Components: 6900 words, 12 figures, 1 table.

Keywords: LAB; receiver function; asthenosphere.

Index Terms: 7208 Seismology: Mantle (1212, 1213, 8124); 7203 Seismology: Body waves; 8120 Tectonophysics: Dynamics of lithosphere and mantle: general (1213).

Received 9 September 2010; **Revised** 9 November 2010; **Accepted** 29 November 2010; **Published** 27 January 2011.

Kumar, P., and H. Kawakatsu (2011), Imaging the seismic lithosphere-asthenosphere boundary of the oceanic plate, *Geochem. Geophys. Geosyst.*, *12*, Q01006, doi:10.1029/2010GC003358.

1. Introduction

[2] Oceanic tectonic plates form at mid-oceanic ridges, and as they spread away from the mid-ocean ridges and cool, they again descend into the mantle along the trenches by subduction. In the plate tectonic hypothesis, the lithosphere is in constant motion over the asthenosphere, a weak zone seismically characterized as a lower-velocity layer. The first seismic observation of the asthenospheric lower-velocity channel was reported by Gutenberg [e.g., *Gutenberg*, 1959] at a depth of ~50–200 km. Therefore, the velocity reduction in the uppermost mantle, similar to the seismic LAB, has been sometimes termed the Gutenberg (G) discontinuity [*Revenaugh and Jordan*, 1991] that may define the top of the low-velocity layer. Elucidating the conditions at the oceanic LAB is, thus, essential for our understanding of plate tectonics that defines the basic framework of the dynamics of our planet. Most

information about the nature of the oceanic lithosphere/asthenosphere system so far, however, comes from surface wave dispersion studies [*Kanamori and Press*, 1970; *Leeds et al.*, 1974; *Zhang and Tanimoto*, 1993; *Ekström and Dziewoński*, 1998; *Nettles and Dziewoński*, 2008] which lack sufficient resolution (>~40 km) vertically as well as horizontally to adequately delineate the fine-scale variations at the bottom of oceanic plates.

[3] Analyzing data from two seafloor borehole broadband seismic observatories, *Kawakatsu et al.* [2009a] showed a sharp LAB around a depth of 60–80 km below oceanic plates, and proposed a model of partially molten asthenosphere consisting of horizontal melt-rich layers embedded in melt-less mantle beneath oceanic region that is now termed a melt-lubricated *millefeuille* asthenosphere model [*Kawakatsu et al.*, 2009b]. This model is originally developed, by incorporating recent experimental and theoretical studies on shear deformations [*Holtzman et al.*, 2003; *Katz et al.*, 2006], to explain the observed strong seismic LAB signals in the presence of a small amount of melt, as such a structure effectively reduces vertically propagating shear wave velocities [*Backus*, 1962]. This model also explains, at least qualitatively, other observations such as the strong radial seismic anisotropy of the low-velocity zone [*Montagner and Tanimoto*, 1991; *Ekström and Dziewoński*, 1998; *Gung et al.*, 2003; *Nettles and Dziewoński*, 2008] as well as the presence of young volcanism in the old normal oceanic plates [*Hirano et al.*, 2006], and assumes that the lithosphere grows with age, unlike other models that assume constant thickness layer [e.g., *Hirth and Kohlstedt*, 1996; *Karato and Jung*, 1998]. Considering that there exist only two localities of seafloor borehole seismic observatories, however, the age dependence of oceanic LAB needs to be further substantiated.

[4] Here, we investigate the oceanic lithosphere using high-resolution body waves for a large number of teleseismic waveforms to map the LAB with unprecedented details. We use mainly shear-to-compressional (*S*-to-*p*) converted waves [*Farra and Vinnik*, 2000; *Kumar et al.*, 2005a, 2006; *Rychert et al.*, 2005] for the purpose. Recently the station-based teleseismic *S*-to-*p* conversion (*S* receiver function) technique has been shown effective to map the uppermost mantle discontinuities such as LAB in continents [*Kumar et al.*, 2005a, 2006; *Rychert et al.*, 2005]. The crustal and uppermost mantle seismic structures for the oceanic environment using high-resolution body waves are scarce due to the absence of ocean based seismometers. There are reports based on data from seismic stations installed in the ocean islands [*Li et al.*, 2004; *Rychert and Shearer*, 2009], but the crustal or uppermost mantle structures there are unlikely to be the exact proxy for the normal oceanic plate.

2. Methodology and Data

[5] In the present study we use the converted wave techniques, namely *P*-to-*s* (*P* receiver function, PRF) [*Burdick and Langston*, 1977; *Langston*, 1977; *Vinnik*, 1977] and *S*-to-*p* (*S* receiver function, SRF) [*Farra and Vinnik*, 2000]. The PRF is a routine technique to decipher the crustal and upper mantle seismic parameters from three-component seismic station utilizing *P*-to-*s* conversions from a discontinuity beneath the seismic station, while the SRF looks for *S*-to-*p* conversions in the teleseismic range. The latter technique proves to be an important tool to detect the upper most mantle discontinuities such as the LAB owing to its advantages over the PRF and thus serves as an important supplement for the former. The advantage of using SRF over PRF is that the former is free from shallow layer multiples in the time window of arrival of main converted *Sp* phases from the deeper discontinuities, whereas in PRF, the converted *Ps* phases and the shallow layer crustal multiples fall in the same side of the time window making the identification of phases ambiguous. Another property of SRF is its larger slowness thus it samples laterally much further distance than PRF. The SRF technique has become an effective tool to map the uppermost mantle discontinuity in diverse tectonic regimes of the world [*Oreshin et al.*, 2002; *Li et al.*, 2004; *Kumar et al.*, 2005b, 2006, 2007; *Rychert et al.*, 2005, 2007; *Sodoudi et al.*, 2006; *Angus et al.*, 2006; *Landes et al.*, 2007].

[6] We use a large number of seismological data from continental stations encompassing diverse geological ages of oceanic crust (Figure 1). We use data from Japanese networks F-net, Hi-net, and from the IRIS DMC. Here, our main motivation is to map the oceanic LAB for a variety of plate age. The objective of our experiment is schematically described in Figure 2. *S* waves coming from the teleseismic distance range, whenever they encounter seismological discontinuities, convert to *P* waves. Since *S* waves have larger slowness compared to *P* waves, the conversion points for *S*-to-*p* waves will be much further away from the seismological stations, thus allowing us to investigate the oceanic plates further away from the station. We also

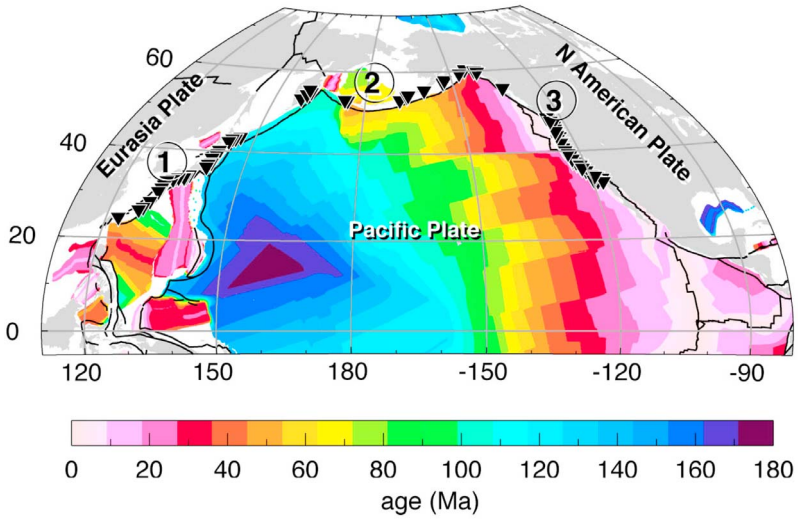

Figure 1. The location of seismic stations (black inverted triangles) whose data are used in the present study. The color indicates the oceanic crustal age of the Pacific region (http://www.ngdc.noaa.gov/mgg/ocean_age/ocean_age_2008.html). The encircled numbers indicate the three major plate boundaries: 1, Japan; 2, Aleutian; 3, North American west coast. The black lines denote plate boundaries.

compare images obtained by the SRFs with those by the PRFs for two regions where dense seismic networks are available (northeast Japan and south California).

[7] We analyze events with a magnitude greater than or equal to 5.6 (mb). For PRF analysis we restrict the events within 35–95° epicenteral distance, while for SRF analysis the events are within 60–85°. For the broadband data from F-net and IRIS, after a 1Hz low-pass filter, we select visually those events which show clear *P* phases at vertical components at around theoretical *P* onset time for the analysis of PRFs. Similarly for SRFs, we select visually those waveforms which show *S* phases at radial components at around theoretical *S* onset. However, for the Hi-net data, which will be used in section 5.1, we do not apply this criterion, since the number of waveforms are too large to inspect visually.

[8] The methods for computing receiver functions are described by *Kumar et al.* [2005a, 2005b, 2006] and *Yuan et al.* [2006]. First, we take all the available data for all the stations used in the present study. Data are filtered with a low-pass filter with a corner frequency of 1 Hz. The vertical and radial components are then rotated into *P* and *SV* components, that are defined to be orthogonal to each other [e.g., *Svenningsen and Jacobsen*, 2004], using the incidence angle of the teleseismic reference phases. Here we search for the optimal angle of rotation such that the amplitude of the *P* (*SV*) component in case of PRF (SRF) is minimized at zero time, the arrival time of the reference phase *P* (*S*). The search for amplitudes is automatic and spanning a time window of ±1 s of the reference phase [*Kumar et al.*, 2005a, 2005b, 2006]. For different RFs, the distributions of the angle of rotation used are shown in Figure 3. In presence of large noise, incidence angles determined in this way may be erroneous. Therefore we discard the events with incidence angles >52°. This coordinate rotation ensures a clean decomposition of *P*-to-*s* (*S*-to-*p*) converted waves from the incident *P* (*S*) wave that is

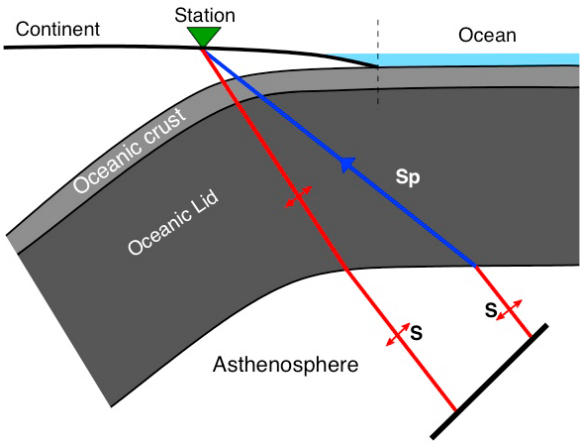

Figure 2. Schematic ray diagram depicting paths for a direct teleseismic *S* wave and a converted *Sp* wave from a discontinuity. The *S* wave is converted to *P* wave at the oceanic LAB and recorded at the seismic station (shown as inverted green triangle) located at the edge of the continent.

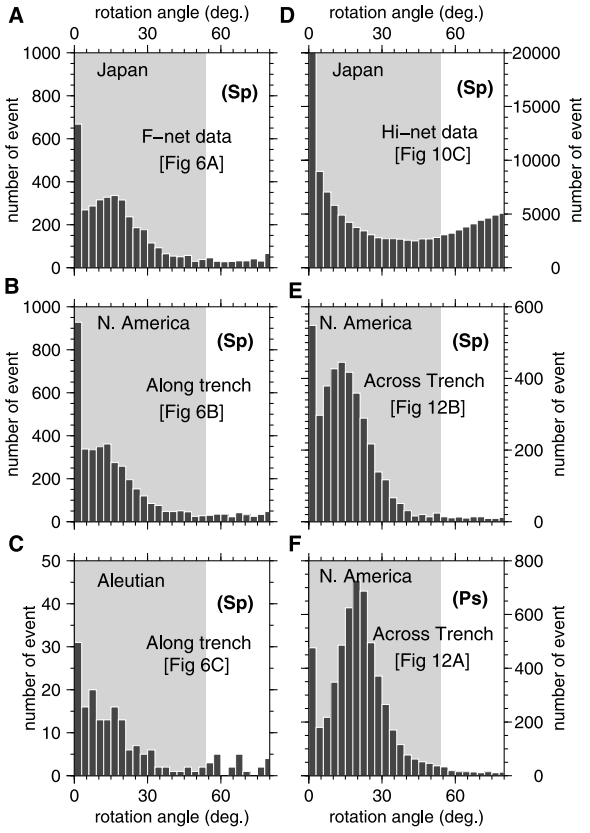

Figure 3. Distribution of events with the angle of incidence estimated based on minimizing the *SV* pulse at *P* component of seismograms for SRF and vice versa for PRF. We have kept threshold angle of incidence to be 52° beyond which events are discarded due to possible contamination by high noise level. The shaded region shows the data at incidence angles less than 52° that are used in the study. (a) Japanese data for SRF. (b) North American data for SRF. (c) Aleutian data for SRF. (d) Japanese Hi-net data used for SRF along trench-perpendicular profiles shown in Figure 10c. (e and f) North American SRF and PRF data used for imaging shown in Figure 12.

useful for imaging. Once the traces are rotated into *P* and *SV* components, then we do the source normalization using deconvolution. We adopted here the time domain deconvolution technique [*Berkhout*, 1977]. In case of PRF, the *SV* is deconvolved with *P* and for SRF, *P* is deconvolved with *SV*. Further, in case of SRF the time series are reversed in order to be able to compare with PRF. *P* and *S* receiver functions thus obtained are then moveout corrected at a reference slowness of 6.4 s/deg.

3. Images of Oceanic LAB

[9] In order to map the oceanic LAB using stations located at the periphery of the ocean-continent margins, we take the advantage of large lateral sampling area of *S*-to-*p* conversions owing to its large slowness (Figure 2). We select only those waveforms whose *S*-to-*p* conversions points are located under the ocean. Data are further limited based on conversion points that are located at fairly horizontal part of the LAB (see Figures 4–5) to ensure that there is not much of the dip effect on the stack. The times of the occurrence of phases in RFs are converted to depth using the IASP91 earth model [*Kennett and Engdahl*, 1991]. Our experimental regions comprise of ocean-continent margins along the Japan, Aleutian and North America plate boundaries (Figure 6) spanning diverse crustal ages in the circum-Pacific belt (Figure 1).

[10] In order to ensure that in Figure 6 the oceanic LABs are taken from well defined relatively flat part of the subducting slab, we take a number of profiles almost trench perpendicular making the trench as the reference point for distance measurement (Figure 4). Along all the profiles we observe a negative phase interpreted as LAB, above which local seismicity within the lithosphere is apparent. Another feature of Figure 5 is that the LABs are in fact the straight part and have not much of contribution from the dipping part.

[11] Figure 6 summarizes the LAB images. The seismic image sections from Japan and North America coherently reveal at least three prominent

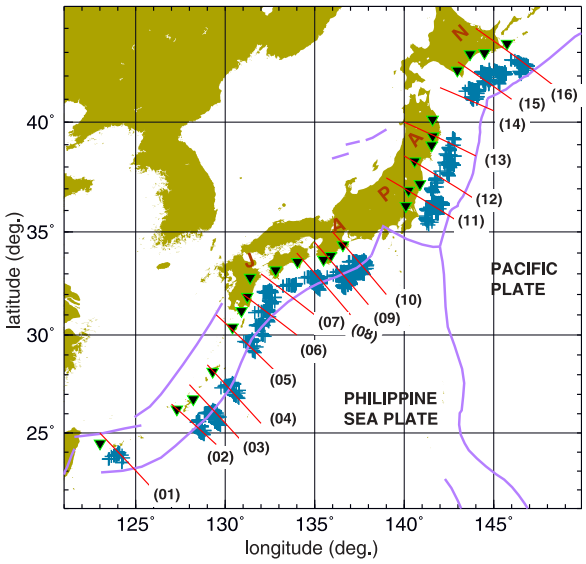

Figure 4. The distribution of conversion points at a depth of 100 km, for *S*-to-*p* along the trench. The red lines are the profiles along which the sections have been analyzed in Figure 5. The numbers with parenthesis indicate the profile numbers. Black inverted triangles are the seismic stations used.

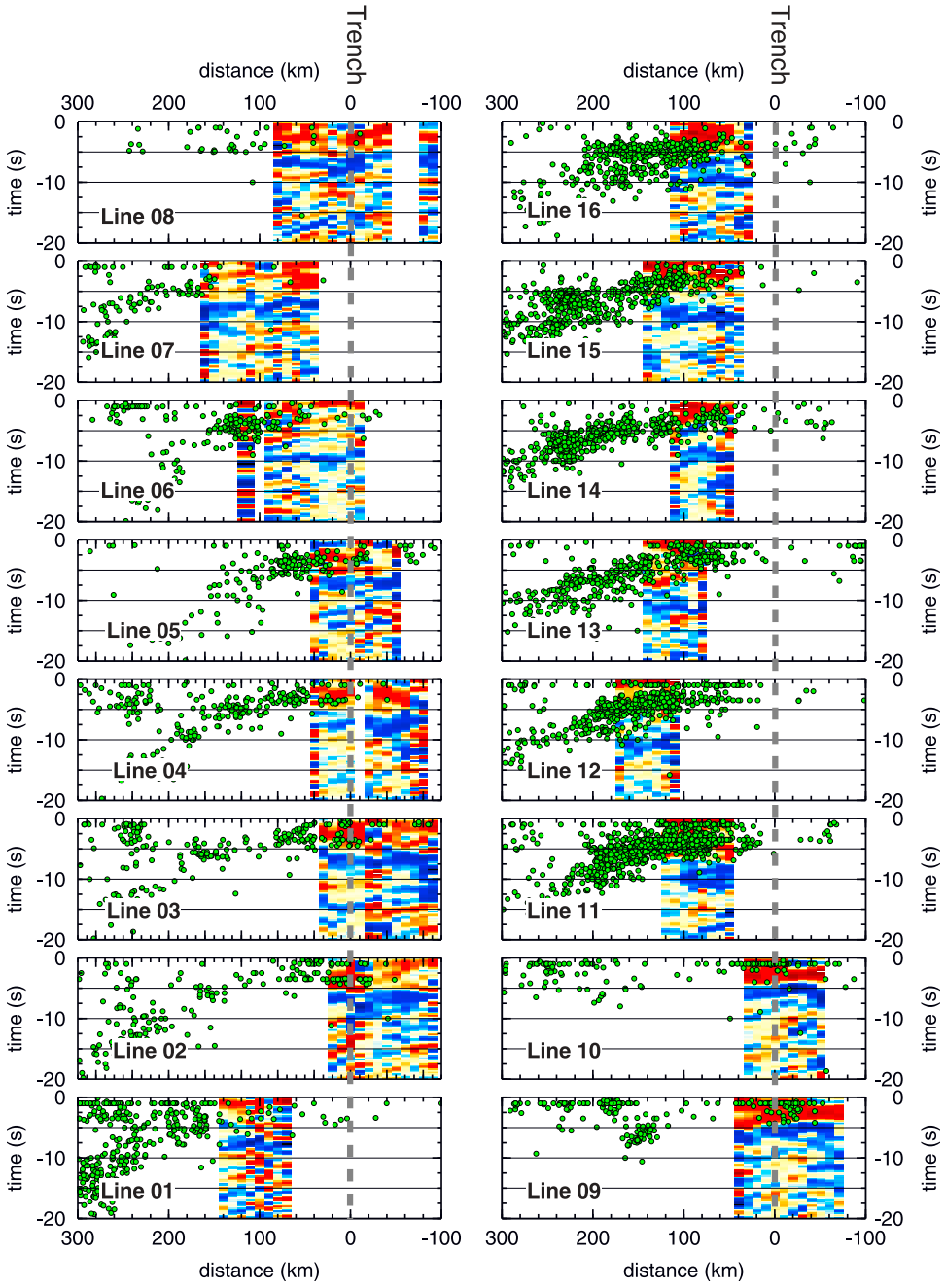

Figure 5. *S* receiver function images along the various profiles shown in Figure 4 with corresponding numbers. The red and blue colors are positive and negative polarities. The blue polarities in all the panels indicate LAB of the subducting plate. It is clear that all the earthquake hypocenters (green dots) are located within the lithosphere above the LAB. The zero in all the sections is the location of trench. The images are generated for the conversion points computed at a depth of 100 km for *S*-to-*p* waves. The purpose of Figure 5 is to show that we select only those data that are representative for the oceanic plates; there is not much appreciable dip observed in the LAB within the analyzed sections in the present work.

phases, positive (red image) within ~5 km that may correspond to the upper interface of subducting slab, another positive within ~12 km corresponding to the oceanic Moho and negative phases (blue image) at ~40–100 km corresponding to the LAB due to the decrease in velocity downward. For the Japanese image, there is a distinct contrast in LAB depths between northeast Japan where the old (~130 Myr) Pacific plate is subducting and southwest Japan where the young (~30–70 Myr)

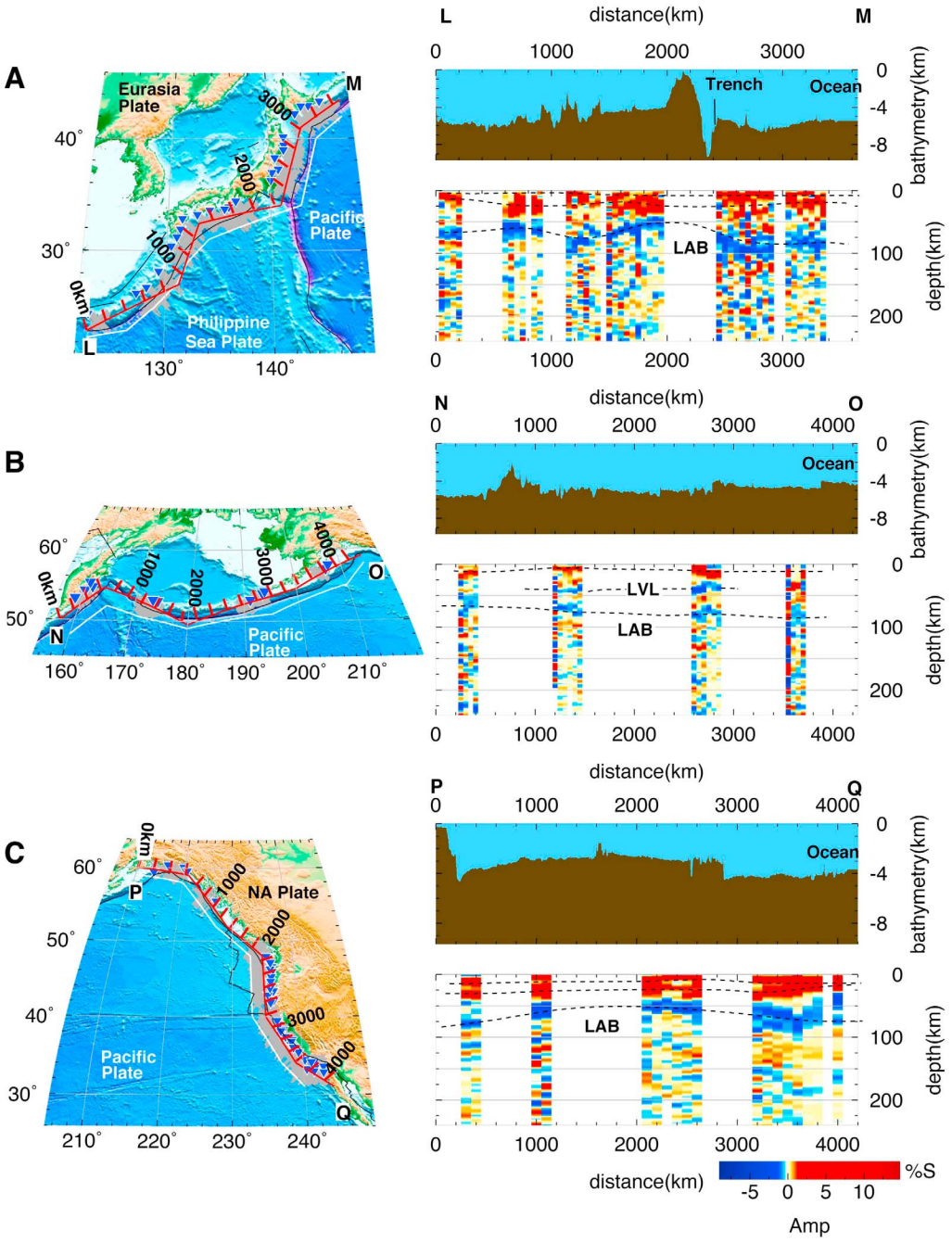

Figure 6. Map of the northern Pacific plate boundary regions and *S* receiver function images: (a) Japan, (b) Aleutian, and (c) North American west coast. In all the maps red lines with ticks are profiles along which the receiver function images are made. The shaded points are the conversion points for *S*-to-*p* waves at 100 km depth, and the inverted blue triangles are the seismic stations. The black lines mark plate boundaries (trench or transform fault). The right-hand panels show the respective *S* receiver function images along the profiles plotted in distance, and the ocean floor bathymetry just seaward of plate boundaries (along the white lines in the maps) is also plotted at the top. In all the images the dashed black lines are the interpreted major seismic discontinuities with red as positive and blue as negative polarities; negative phases in blue colors occur at about ~40 to 100 km interpreted as LAB.

Table 1. The Thickness of the Oceanic Lithosphere and the Corresponding Age for the Generation of Figure 9[a]

Region	Subregion	Age (Myr)	LAB Depth (km)	Error (km)	Depth of Slab Top (km)	Depth of First Phase (km)	Error (km)	Plate Thickness 1 (km)	Plate Thickness 2 (km)	Reference[b]
Japan	I	50	71.8	1.1	13	5.4	2.5	58.8	66.4	R1
	II	73	65.3	5.3	4.5	1.8	1.8	60.8	63.5	Rb
	III	30	88.7	9.9	3.5	4.5	2.7	85.2	84.2[c]	Rb
	IV	30	55.3	7.3	3.5	5.4	0.2	51.8	49.9	Rb
	V	126	87.1	5.8	16	5.4	0.3	71.1	81.7	R2
	VI	130	94.8	9.9	21	7.2	1.4	73.8	87.6	R3
	VII	128	82.3	9.4	13	5.4	1.4	69.3	76.9	R4
Aleutian	I	100	65.3	8.9	-[d]	3.6	3.7	-	61.7[c]	-
	II	70	70.8	2.6	6.1	7.2	1.6	64.7	63.6	Rb
	III	60	78.3	4.3	20	14.4	1.7	58.3	63.9	R5
	IV	52	92.9	6.6	16	18.0	4.1	76.9	74.9	R6
North American west coast	I	31	78	3.6	11.6	10.8	0.2	66.4	67.2	R7
	II	20	60.8	8	1.3	3.6	1.2	59.5	57.2	Rb
	III	9	51.9	5.3	2.0	7.2	1.9	49.9	44.7	Rb
	IV	12	53.3	3.9	2.0	5.4	0.4	51.3	47.9	Rb
	V	27	56.3	10.3	3.4	5.4	1.6	52.9	50.9	Rb
	VI	32	62.1	2.6	3.0	6.3	0.7	59.1	55.8	Rb
	VII	33	82.1	9.7	3.5	7.2	1.2	78.6	74.9	Rb
	VIII	20	72.3	4	2.7	9.0	0.5	69.6	63.3	Rb
NW Pacific[e]	WP1[f]	25	55	-	-	-	-	-		-
	WP1[g]	49	76	1.8	-	-	-	-		-
	WP2	129	82	4.4	-	-	-	-		-

[a]The estimated errors (2σ) are shown wherever available. The subregions are shown in Figure 7.
[b]R1, *Wang et al.* [2001]; R2, *Mochizuki et al.* [2008]; R3, *Miura et al.* [2005]; R4, *Iwasaki et al.* [1988]; R5, *Holbrook et al.* [1999]; R6, *Ye et al.* [1997]; R7, *Brocher et al.* [1994]; Rb, ocean floor bathymetry is used.
[c]Seamount is subducting around this region.
[d]No slab structure is available.
[e]From *Kawakatsu et al.* [2009a].
[f]Parece-Vela basin.
[g]Western Philippine Sea plate.

Philippine Sea plate is subducting. The estimated LAB depth of the oceanic plate (Table 1) in northeast Japan is ~80–95 km, while those in southwest is ~55–70 km (except for one section where the effect of subducting seamounts observed in the ocean bathymetry appears to be causing the thickening, Figure 6a). It is unlikely that this contrast is due to the effect of dip of subduction caused by the difference in the distance from trench that each section is taken (Figure 5). In the North American west coast the situation appears to be similar: where the newly born (~10 Myr) Juan de Fuca plate is subducting, the LAB depth is ~50 km, but where ~30 Myr Pacific plate is subducting, it becomes >55 km. For Aleutian region, the LAB depths increase from west to east, partly reflecting the increase of the distance from the trench.

4. Thickness of Oceanic Plates

[12] In order to estimate the thickness of the oceanic lithospheres we divide the studied regions based on the conversion points at a depth of 100 km for *S*-to-*p* waves (Figure 7) and generate receiver function stacks (Figure 8). The stacked regions are chosen considering the similarity of LAB signals in RFs and the similarity of the plate age. The frequency has been kept high (low-pass filtered at a corner frequency of 1 Hz). We clearly see within ~2 s first positive peaks that are sometimes followed by another positive peak. In case where there are two positive peaks the first one is interpreted as a signal from the top of the oceanic lithosphere. Following these, negative peaks are well observed above the $\pm 2\sigma$ error bounds that are interpreted as LAB signals.

[13] The depths of the top of the (subducting) oceanic plate are estimated directly either from published literatures on active source surveys [*Wang et al.*, 2001; *Mochizuki et al.*, 2008; *Miura et al.*, 2005; *Iwasaki et al.*, 1988; *Nakanishi et al.*, 2009; *Holbrook et al.*, 1999; *Ye et al.*, 1997; *Brocher et al.*, 1994] when the corresponding conversion points of LAB signals are located beneath the subduction zone, or from the ocean floor bathymetry (http://www.ngdc.noaa.gov/mgg/global/global.html) when the conversion points are

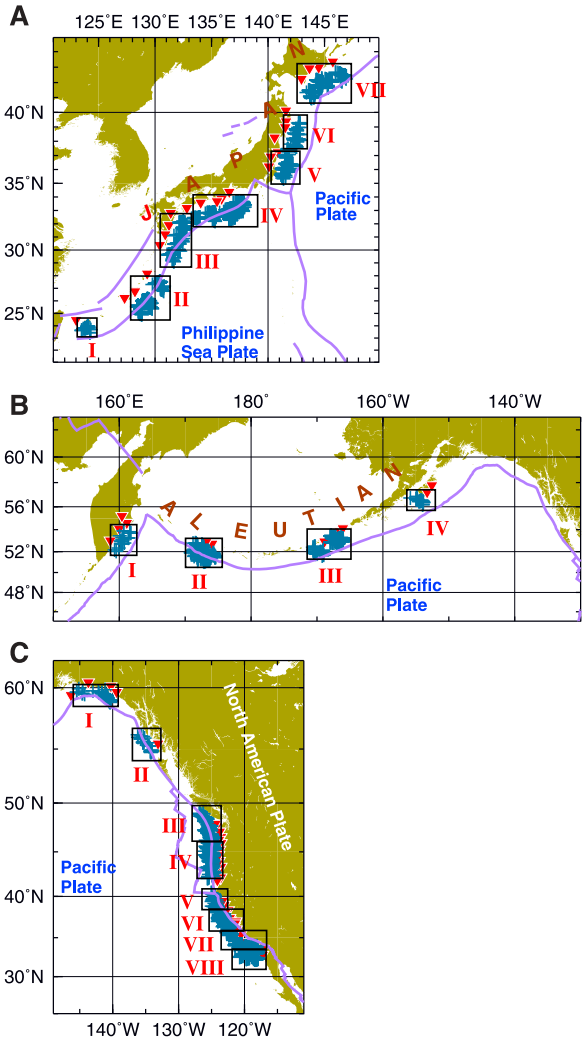

Figure 7. Conversion points of the *S*-to-*p* phase at a depth of 100 km are shown in blue cross for (a) Japan, (b) Aleutian, and (c) North American west coast plate boundaries. The inverted red triangles are the seismic stations whose data have been used in the present study. The piercing points are grouped into several bins indicated by black rectangles with number in roman letters for each region. From each bin the data are used for stacking to estimate the depths of the LABs and for the error analysis shown in Figure 8.

located near or seaward of trenches (or plate boundaries). The difference of these depth estimates and the LAB depths given above are used in Table 1 and Figure 9a as the plate thickness (plate thickness 1). We note that the estimates based on the bathymetry may overestimates the actual thickness slightly as we do not account for the sediment layer.

[14] Table 1 summarizes the results where nominal standard errors for the depth determination estimated by bootstrap are also given. Considering that fore-arc regions of subduction zones can be highly laterally heterogeneous, the actual error should be larger. If we vary the average *P* wave speed from 4.0 km/s to 5.8 km/s and *Vp*/*Vs* ratio from 1.6 to 1.9 for the top 10 km, the time difference between direct *S* and *S*-to-*p* converted waves would vary about 1.4 s, which may translate into ~13 km difference in the depth estimate. Although it is difficult to assess the exact possible error, ~10 km might give a reasonable range. Considering this uncertainty, as for an alternative measure of the plate thickness, we use the depth of the top of oceanic lithosphere estimated from the aforementioned first positive phase of RFs. While this measure reduces the errors due to local velocity variations, the lateral distance between two conversion points (i.e., top and bottom of the plate) may introduce an additional source of error. The plate thicknesses estimated this way are given in Table 1 (plate thickness 2) and shown in Figure 9b.

5. Discussion

5.1. Comparison of *P* and *S* Receiver Function Images Along Profiles Perpendicular to Plate Boundaries

[15] To ensure the robustness of the images obtained using *S* receiver functions, we compare detailed images perpendicular to plate boundaries obtained from both PRF and SRF where dense networks are available (i.e., in Japan and southern California). For Japan we use dense data from Hi-net (Figure 10) and for North America we use data from IRIS (Figures 11 and 12) in order to construct images along the profiles almost perpendicular to the plate boundaries. The PRF images of the bottom of the subducting plate beneath northeast Japan have been reported by *Tonegawa et al.* [2006] and *Kawakatsu et al.* [2009a] (Figure 10b). To obtain corresponding SRF images, a high pass filter with a corner frequency of 0.1 Hz is used. If we compare the PRF (Figure 10b) and SRF (Figure 10c) then it is clear that SRF has lower frequency than PRF, so in SRF we do not get much details as observed in PRF (Figure 10). However, the fundamental discontinuities such as oceanic Moho (red: positive) and LAB (blue: negative) are well observed in both the independent techniques with consistency. Also the above phases are well matching with the observations in Figure 6.

[16] In case of North American profile (shown in Figure 11), we observe, in both PRF (Figure 12a)

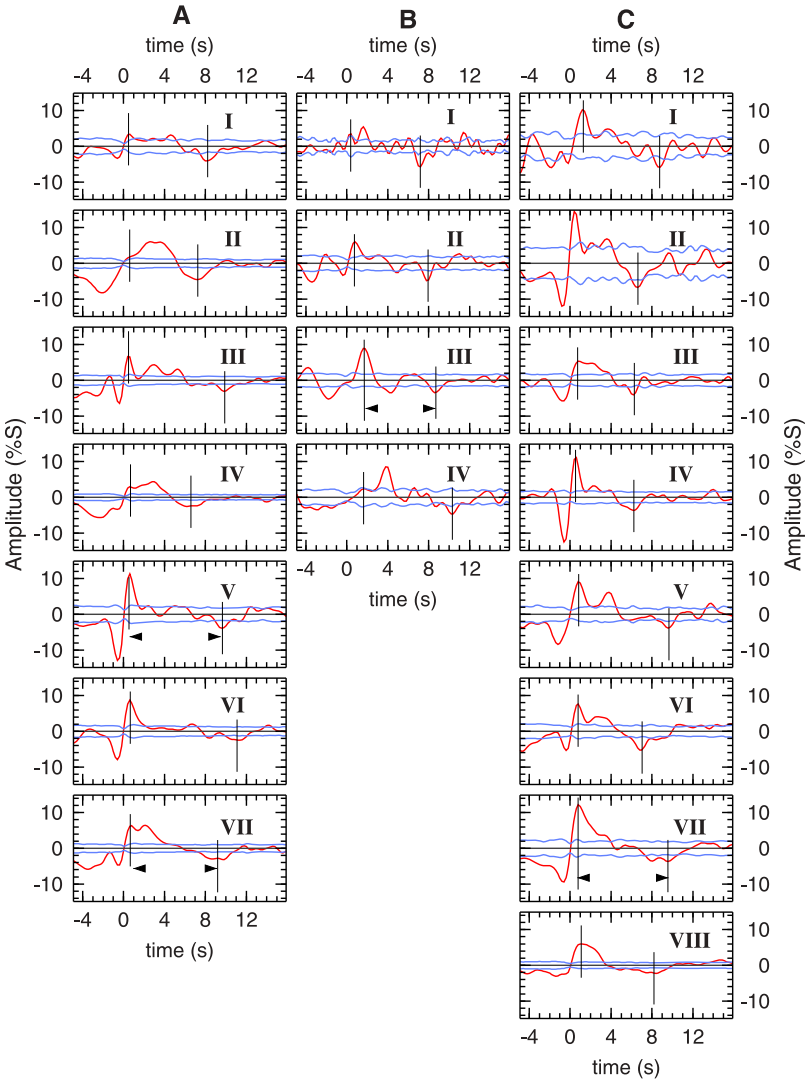

Figure 8. Stacked SRFs for the groups shown in Figure 7 for different regions: (a) Japanese subduction zone, (b) Aleutian, and (c) North American region. The two blue lines running parallel to the mean lines are the $\pm 2\sigma$ error bounds. The first positive polarity marked by the vertical solid lines are the top of the oceanic crust and the negative phases occurring within ~4 to ~11 s are LAB signals.

and SRF images (Figure 12a), two positive phases (in red) within 6 s of window corresponding to ~20–50 km depth and another a coherent negative phases gently deepening toward continental side from ~5 s (~45 km) to ~8 s (72 km) interpreted as LAB. The continuity of the LAB from ocean to continental inland is remarkable and deserves further attention that is beyond the scope of this paper. The continental LAB at a depth of 72 km may be comparable to the top of the high attenuation zone observed by surface wave analysis [*Yang and Forsyth*, 2008]. In both regions, we find the consistency of images obtained by the independent techniques that assures the robustness of the SRF images of this work.

5.2. Thickness Versus Age

[17] Figure 9 compares the observed plate thickness with age, suggesting that the seismologically determined plate thickness shows a considerable scatter of about ±15 km, however the general trend in the data shows an asymptotic increase, in agreement with the thermally predicted models. Smaller the lithospheric age, smaller its thickness. For example, the average thicknesses are 59.4 ± 9.4 (std. dev.) (for thickness 1 in Table 1; 56.7 ± 9.4 for thickness 2) for 0–40 Myr seafloor; 65.9 ± 8.5 (68.1 ± 5.8) for 40–100 Myr seafloor; and 74.1 ± 5.6 (82.1 ± 4.4) for 100–130 Myr seafloor, if we discard two localities where subduction of the bathymetry highs is inferred (circled by dashed

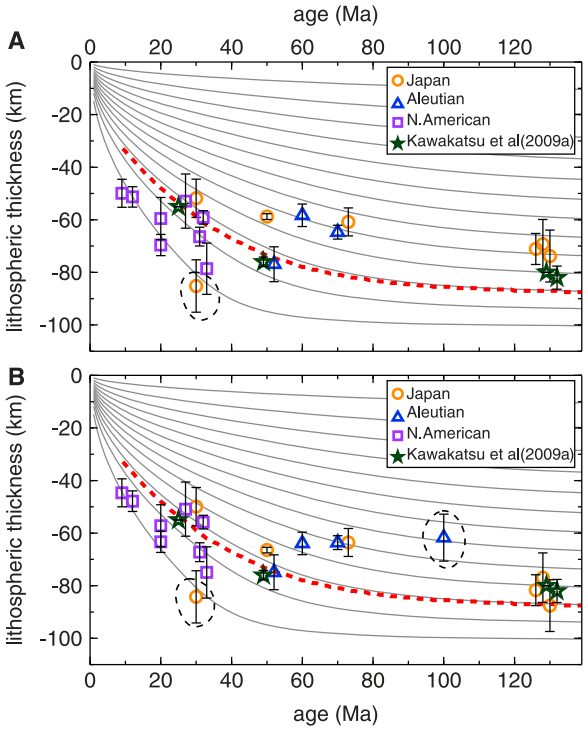

Figure 9. Observed plate thicknesses of oceanic lithospheres are plotted against their age for (a) plate thickness 1 and (b) plate thickness 2 in Table 1. Different color symbols denote data from different geographical regions, and symbols are slightly displaced horizontally when they overlap to make them more visible in the plot. Isotherms (gray contour lines with a 100° interval) and the estimated top of partial melting region (red dashed contour line) are taken from *Kawakatsu et al.* [2009a]. Dashed circles enclosing data belong to the region where subducting seamounts are seen in the bathymetry (Table 1) and thus may not be representative of the normal oceanic lithosphere.

lines in Figure 9). This trend appears more evident for the Japanese and North American plate boundaries when they are grouped separately (note that Aleutian IV (52 Myr) is not so far from North America I (31 Myr)). The increase of thickness for the age of the first ~30–40 Myr appears more pronounced compared to the rest where it tends to remain nearly constant that appears to be consistent with surface wave results [*Forsyth*, 1975].

[18] Although the general trend of plate thickening with age seems evident in Figure 9, the rate of thickening appears much more gentle compared the trend in the isotherms predicted by thermal models [e.g., *Stein and Stein*, 1992; *Kawakatsu et al.*, 2009a], and it may be argued that, considering the scatter in data points, the thickness variation after 20 Myr can be explained as well by a constant thickness model [e.g., *Hirth and Kohlstedt*, 1996; *Karato and Jung*, 1998]. Here we simply point out that the model predicts that the plate thickness to be constant from the birth, which does not seem to be consistent with our data. We also list other possible causes of the bias or the scatter in data. First, we note that for younger plates which tend to be warmer and slower in seismic velocity, the LAB depth tends to be overestimated by using the 1-D reference velocity model. Second, considering the

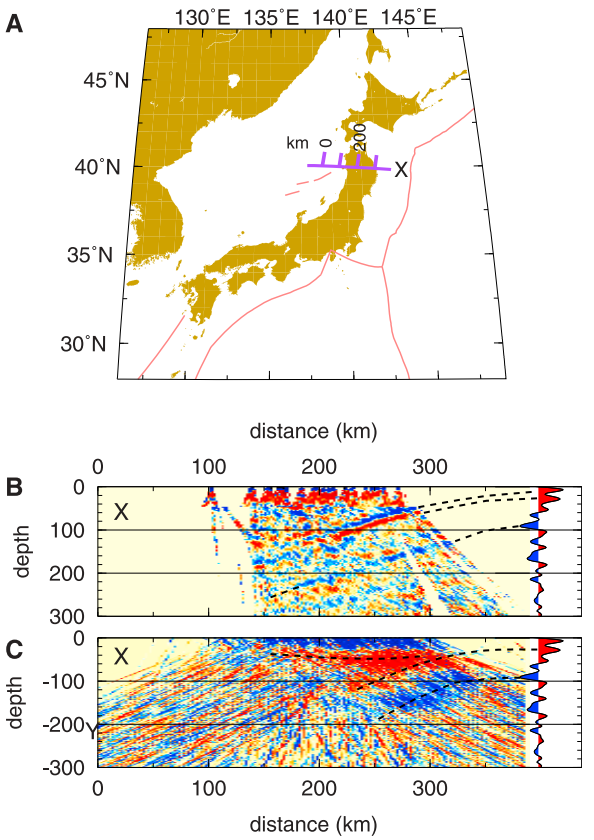

Figure 10. (a) *P* and *S* receiver function images along the profile X marked using the data from continental stations. (b) PRF image from *Kawakatsu et al.* [2009a]. (c) SRF images along the same profile X. The wiggle trace in the right side in each plot shows the stacked SRF of the data falling at the end of the profile and generated from the data from trench side shown in Figure 5; large positive and negative peaks are above the noise level and correspond well to the top and bottom images of the subducting plate, while other smaller peaks are not seen coherently in the adjacent regions. All the images show consistent results revealing the subducted Pacific plate along the trench. The SRF image (Figure 10c) does not show the details as observed in PRF (Figure 10b) due to the much lower frequency content of the data. The data used in the sections are from Japanese network Hi-net. This also emphasizes that our observation of LAB is robust as they bear remarkable consistence.

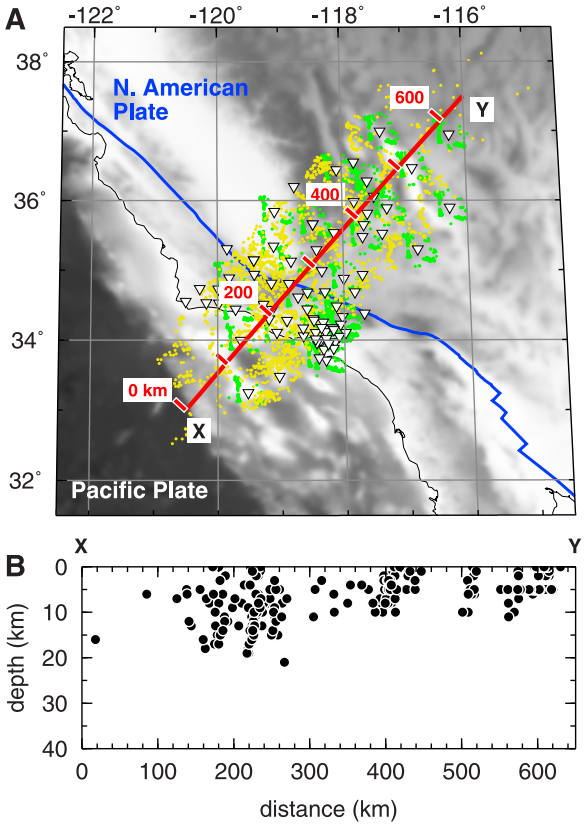

Figure 11. (a) The map of a subregion in the North American plate margin where we have analyzed the seismic sections perpendicular to the San Andreas transform fault to ensure the robustness of LAB observation. The red line shows the profile (XY) with tick marks for distance. Inverted triangles denote seismic stations. The green and yellow dots are the conversion points for *P*-to-*s* and *S*-to-*p* at 100 km depth, respectively. The blue curve indicates the San Andreas Fault. (b) The depth section of the seismicity in the region along the profile shows that all earthquakes are located within 25 km depth.

limited ray back-azimuth coverage of this study, the azimuthal anisotropy in the lithosphere and/or asthenosphere may affect the LAB depth estimate significantly. Third, regional variations of *Vp*/*Vs* ratio in the lithosphere may also contribute to the scatter. When we fully incorporate these effects, a simpler trend may become resolved.

[19] The thickness of plate estimated from the seismic LABs is generally consistent with the notion that the plate evolution is controlled by its cooling [e.g., *Stein and Stein*, 1992], and thus the seismic LAB that may define the bottom of the oceanic plate or the top of the asthenosphere has thermal origin and deepens with age. This view is consistent with the model advocated by *Kawakatsu et al.* [2009a], although there exists a significant scatter in the data requiring additional controlling factors. Further attempts of mapping of the seismic LAB utilizing other seismological techniques are awaited.

6. Conclusion

[20] By means of the *S* receiver function technique, images of the oceanic LABs along three margins of oceanic plates whose crustal age ranges from ~10 Myr to ~130 Myr are obtained. The thickness of oceanic plate estimated from LABs increases with the age of oceanic plate. The seismologically observed oceanic LAB thus represents a boundary that grows with age, providing a tight constraint on its origin.

Acknowledgments

[21] P.K. is supported by the JSPS fellowship provided by the Japan Society for the Promotion of Science. PK is also grateful to the Director, NGRI and DG, CSIR for granting him leave and to X. Yuan for the *Sp* CCP stacking code. Earlier comments on the manuscript by S. Honda and G. Helffrich were helpful. We thank Don Forsyth and Peter Shearer for enthusiastic reviews and an anonymous reviewer for constructive comments. This work is partly supported by Grant-in-Aid for Scientific

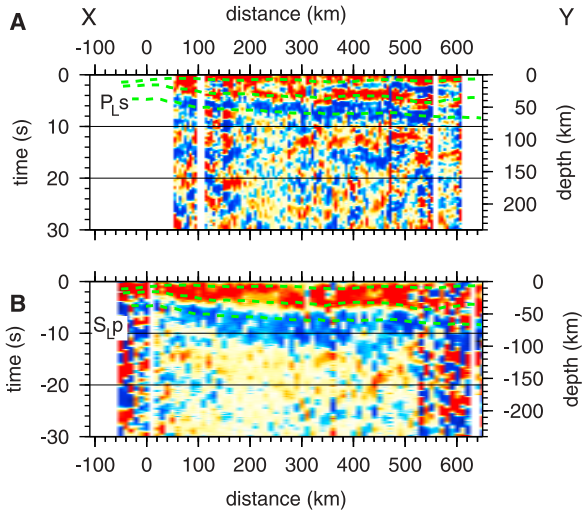

Figure 12. (a) PRF image and (b) SRF image along the profile XY shown in Figure 11. The positive and negative polarities are indicated by red and blue colors, respectively. The negative LAB phases marked PLs and SLp show consistent images obtained by the independent techniques. RF images are plotted at a location where the *S*-to-*p* conversion point is located at a depth of 100 km. Green broken lines in Figures 12a and 12b mark the same two positive and one negative signatures observed in both PRF and SRF images.

Research 22000003 through JSPS. The data are from DMC from IRIS, F-net, and Hi-net from Japan. Analysis has been done with Seismic Handler (K. Stammler), and figures are produced using GMT [*Wessel and Smith*, 1998].

References

Angus, D. A., D. C. Wilson, E. Sandvol, and J. F. Ni (2006), Lithospheric structure of the Arabian and Eurasian collision zone in eastern Turkey from *S* wave receiver functions, *Geophys. J. Int.*, *166*, 1335–1346.

Backus, G. E. (1962), Long-wave elastic anisotropy produced by horizontal layering, *J. Geophys. Res.*, *67*, 4427–4440.

Berkhout, A. J. (1977), Least square inverse filtering and wavelet decomposition, *Geophysics*, *42*, 1369–1383.

Brocher, T. M., G. S. Fuis, M. A. Fisher, G. Plafker, M. J. Moses, J. J. Taber, and N. I. Christensen (1994), Mapping the megathrust beneath the northern Gulf of Alaska using wide-angle seismic data, *J. Geophys. Res.*, *99*, 11,663–11,685.

Burdick, L. J., and C. Langston (1977), Modeling crustal structure through the use of converted phases in teleseismic body-wave forms, *Bull. Seismol. Soc. Am.*, *67*, 677–691.

Ekström, G., and A. M. Dziewoński (1998), The unique anisotropy of the Pacific upper mantle, *Nature*, *394*, 168–172.

Farra, V., and L. Vinnik (2000), Upper mantle stratification by *P* and *S* receiver functions, *Geophys. J. Int.*, *141*, 699–712.

Forsyth, D. W. (1975), The early structural evolution and anisotropy of the oceanic upper mantle, *Geophys. J. R. Astron. Soc.*, *43*, 103–162.

Gung, Y., M. Panning, and B. Romanowicz (2003), Global anisotropy and the thickness of continents, *Nature*, *442*, 707–711.

Gutenberg, B. (1959), *Physics of the Earth's Interior*, Elsevier, New York.

Hirano, N., et al. (2006), Volcanism in response to plate flexure, *Science*, *313*, 1426–1428.

Hirth, G., and D. Kohlstedt (1996), Water in the oceanic upper mantle: Implications for rheology melt extraction and the evolution of the lithosphere, *Earth Planet. Sci. Lett.*, *144*, 93–108.

Holbrook, W. S., D. Lizarralde, S. McGeary, N. Bangs, and J. Diebold (1999), Structure and composition of the Aleutian island arc and implications for continental crustal growth, *Geology*, *27*, 31–34.

Holtzman, B. K., D. L. Kohlstedt, M. E. Zimmerman, F. Heidelbach, T. Hiraga, and J. Hustoft (2003), Melt segregation and strain partitioning: Implications for seismic anisotropy and mantle flow, *Science*, *301*, 1227–1230.

Iwasaki, T., H. Shiobara, A. Nishizawa, T. Kanazawa, K. Suyehiro, N. Hirata, T. Urabe, and H. Shimamura (1988), A detailed subduction structure in the Kuril trench deduced from ocean bottom seismographic refraction studies, *Tectonophysics*, *165*, 315–336.

Kanamori, H., and F. Press (1970), How thick is the lithosphere?, *Nature*, *226*, 330–331.

Karato, S., and H. Jung (1998), Water, partial melting and the origin of seismic low velocity and high attenuation zone in the upper mantle, *Earth Planet. Sci. Lett.*, *157*, 193–207.

Katz, R. F., M. Spiegelman, and B. Holtzman (2006), The dynamics of melt and shear localization in partially molten aggregates, *Nature*, *442*, 676–679, doi:10.1038/nature05039.

Kawakatsu, H., P. Kumar, Y. Takei, M. Shinohara, T. Kanazawa, E. Araki, and K. Suyehiro (2009a), Seismic evidence for sharp lithosphere-asthenosphere boundaries of oceanic plates, *Science*, *324*, 499–502.

Kawakatsu, H., A. Takeo, Y. Takei, and P. Kumar (2009b), Seismological consequences and observability of melt-lubricated (millefeuille) asthenosphere and a LAB above, *Eos Trans. AGU*, *90*(52), Fall Meet. Suppl., Abstract DI11A–03.

Kennett, B. L. N., and E. R. Engdahl (1991), Travel times for global earthquake location and phase identification, *Geophys. J. Int.*, *105*, 429–465.

Kumar, P., et al. (2005a), The lithosphere asthenosphere boundary in the North–West Atlantic region, *Earth Planet. Sci. Lett.*, *236*, 249–257.

Kumar, P., X. Yuan, R. Kind, and G. Kosarev (2005b), The lithosphere-asthenosphere boundary in the Tien Shan-Karakoram region from *S* receiver functions: Evidence for continental subduction, *Geophys. Res. Lett.*, *32*, L07305, doi:10.1029/2004GL022291.

Kumar, P., X. Yuan, R. Kind, and J. Ni (2006), Imaging the collision of the Indian and Asian lithospheric plates eneath Tibet, *J. Geophys. Res.*, *111*, B06308, doi:10.1029/2005JB003930.

Kumar, P., X. Yuan, M. R. Kumar, R. Kind, X. Li, and R. K. Chadha (2007), The rapid drift of the Indian tectonic plate, *Nature*, *449*, 894–897.

Landes, M., J. R. R. Ritter, and P. W. Readman (2007), Proto-Iceland plume caused thinning of Irish lithosphere, *Earth Planet. Sci. Lett.*, *255*, 32–40.

Langston, C. A. (1977), Corvallis, Oregon, crustal and upper mantle structure from teleseismic *P* and *S* waves, *Bull. Seismol. Soc. Am.*, *67*, 713–724.

Leeds, A. R., L. Knopoff, and E. G. Kausel (1974), Variations of upper mantle structure under the Pacific Ocean, *Science*, *186*, 141–143.

Li, X., R. Kind, X. Yuan, I. Wölbern, and W. Hanka (2004), Rejuvenation of the lithosphere by the Hawaiian plume, *Nature*, *427*, 827–829.

Miura, S., N. Takahashi, A. Nakanishi, T. Tsuru, S. Kodaira, and Y. Kaneda (2005), Structural characteristics off Miyagi forearc region, the Japan trench seismogenic zone, deduced from a wide-angle reflection and refraction study, *Tectonophysics*, *407*, 165–188.

Mochizuki, K., T. Yamada, M. Shinohara, Y. Yamanaka, and T. Kanazawa (2008), Weak interplate coupling by seamounts and repeating M~7 earthquakes, *Science*, *321*, 1194–1197.

Montagner, J. P., and T. Tanimoto (1991), Global upper-mantle tomography of seismic velocities and anisotropy, *J. Geophys. Res.*, *96*, 20,337–20,351.

Nakanishi, A., et al. (2009), Crustal evolution of the south-western Kuril Arc, Hokkaido Japan, deduced from seismic velocity and geochemical structure, *Tectonophysics*, *472*, 105–123.

Nettles, M., and A. M. Dziewoński (2008), Radially anisotropic shear velocity structure of the upper mantle globally and beneath North America, *J. Geophys. Res.*, *113*, B02303, doi:10.1029/2006JB004819.

Oreshin, S., L. Vinnik, D. Peregoudov, and S. Roecker (2002), Lithosphere and asthenosphere of the Tien Shan imaged by *S* receiver functions, *Geophys. Res. Lett.*, *29*(8), 1191, doi:10.1029/2001GL014441.

Revenaugh, J., and T. H. Jordan (1991), Mantle layering from *ScS* reverberations: 3. The upper mantle, *J. Geophys. Res.*, *96*, 19,781–19,810.

Rychert, C. A., and P. M. Shearer (2009), A global view of the lithosphere-asthenosphere boundary, *Science*, *324*, 495, doi:10.1126/science.1169754.

Rychert, C. A., K. M. Fischer, and S. Rondenay (2005), A sharp lithosphere-asthenosphere boundary imaged beneath eastern North America, *Nature*, *436*, 542–545, doi:10.1038/nature03904.

Rychert, C. A., S. Rondenay, and K. M. Fischer (2007), *P*-to-*S* and *S*-to-*P* imaging of a sharp lithosphere-asthenosphere boundary beneath eastern North America, *J. Geophys. Res.*, *112*, B08314, doi:10.1029/2006JB004619.

Sodoudi, F., X. Yuan, Q. Liu, R. Kind, and J. Chen (2006), Lithospheric thickness beneath the Dabie Shan, central eastern China from *S* receiver functions, *Geophys. J. Int.*, *166*, 1363–1367.

Stein, C. A., and S. Stein (1992), A model for the global variation in oceanic depth and heat flow with lithospheric age, *Nature*, *359*, 123–129.

Svenningsen, L., and B. H. Jacobsen (2004), Comment on "Improved inversion for seismic structure using transformed, *S* wavevector receiver functions: Removing the effect of the free surface" by Anya Reading, Brian Kennett, and Malcolm Sambridge, *Geophys. Res. Lett.*, *31*, L24609, doi:10.1029/2004GL021413.

Tonegawa, T., K. Hirahara, T. Shibutani, and N. Fujii (2006), Lower slab boundary in the Japan subduction zone, *Earth Planet. Sci. Lett.*, *247*, 101–107.

Vinnik, L. P. (1977), Detection of waves converted from *P* to *SV* in the mantle, *Phys. Earth Planet. Inter.*, *15*, 39–45.

Wang, T. K., K. McIntosh, Y. Nakamura, C.-S. Liu, and H.-W. Chen (2001), Velocity-interface structure of the southwestern Ryukyu subduction zone from EW9509-1 OBS/MCS Data, *Mar. Geophys. Res.*, *22*, 265–287.

Wessel, P., and W. H. F. Smith (1998), New, improved version of genetic mapping tools released, *Eos Trans. AGU*, *79*(47), 579.

Yang, Y., and D. W. Forsyth (2008), Attenuation in the upper mantle beneath southern California: Physical state of the lithosphere and asthenosphere, *J. Geophys. Res.*, *113*, B03308, doi:10.1029/2007JB005118.

Ye, S., E. R. Flueh, D. Klaeschen, and R. von Huene (1997), Crustal structure along the EDGE transect beneath the Kodiak shelf off Alaska derived from OBH seismic refraction data, *Geophys. J. Int.*, *130*, 283–302.

Yuan, X., R. Kind, X. Li, and R. Wang (2006), The *S* receiver functions: Synthetics and data example, *Geophys. J. Int.*, *165*, 555–564.

Zhang, Y.-S., and T. Tanimoto (1993), High-resolution global upper mantle structure and plate tectonics, *J. Geophys. Res.*, *98*, 9793–9823.